CHALMERS
UNIVERSITY OF TECHNOLOGY

Scattering Center Modelling and Analysis of Traffic Objects

Master's thesis in Communication Engineering

Tingting Liu and Bozhi Bao

Department of Electrical Engineering
CHALMERS UNIVERSITY OF TECHNOLOGY
Gothenburg, Sweden 2017

Master's thesis 2017:NN

Scattering Center Modelling and Analysis of Traffic Objects

TINGTING LIU and BOZHI BAO

CHALMERS
UNIVERSITY OF TECHNOLOGY

Department of Electrical Engineering
Division of Communication systems
Chalmers University of Technology
Gothenburg, Sweden 2017

Scattering Center Modelling and Analysis of Traffic Objects
TINGTING LIU and BOZHI BAO

Supervisor in VCC: Iman Vakili, Sensor A & V Department
Examiner at Chalmers: Henk Wymeersch, Department of Electrical Engineering
Supervisor at Chalmers: Mohammad Ali Nazari

Master's Thesis 2017:NN
Department of Electrical Engineering
Division of Communication systems
Chalmers University of Technology
SE-412 96 Gothenburg
Telephone +46 31 772 1000

Typeset in LaTeX
Printed by [Name of printing company]
Gothenburg, Sweden 2017

Scattering Center Modelling and Analysis of Traffic Objects
TINGTING LIU and BOZHI BAO
Department of Electrical Engineering
Chalmers University of Technology

Abstract

The combination of SAR (synthetic aperture radar) and FMCW (frequency modulation continuous wave) technology offers a high-accuracy, cost-effective imaging sensor for remote sensing. Instead of treating the target as a continuous object, this technology sees the target as several scattering points with certain amplitude which depend on the reflecting intensity. In this thesis, we implement two image reconstruction techniques: Gridding method (widely used in medical imaging) and unequally spaced FFTs (has advantages for arbitrary sampling geometries) to set up the scattering centers model. Then taking account of efficiency and saving time for further data process in self-driving area, only a few of the scattering centers having stronger amplitudes will be kept by doing sparse representation technology. Here, we choose the iterative soft thresholding algorithm based on l_1-norm minimization to fulfill sparse representation. We then discuss the trade-off between the choice of threshold and the number of iterations for the optimization problem to converge.

Keywords: FMCW, SAR, Gridding method, unequally spaced FFTs, sparse representation, l_1-norm minimization, iterative soft thresholding algorithm.

Acknowledgements

Throughout the thesis work many people have offered help to us, without them we can never go that far. The experience of working in VCC Active Safety department is a great treasure for us. We would first like to thank our thesis supervisor Iman Vakili in Volvocar Corporation and our thesis examiner Henk Wymeersch at Chalmers. During the time we were doing the thesis project in Volvocar, Iman as a radar expert always say all he knows and say it without reserve. Whenever we have questions and doubt, Iman is always be there to help us and guide us with some new ideas. Also thanks to Professor Wymeersch, he makes us believe that Chalmers will always be our strong backup force. During the time we were stuck in some problems, Henk did anything he could help us to find out the problems including introducing experts in specific area.

We would also like to express our thankfulness to the teachers and our thesis supervisor Mohammad Ali Nazari at Chalmers who have nonnegligible and irreplaceable function during our master education and thesis report writing.

Finally, We must express our very profound gratitude to our parents for providing us with unfailing support and continuous encouragement throughout our years of studying and through the process of researching and writing this thesis. This accomplishment would not have been possible without them. Thank you.

Tingting Liu and Bozhi Bao, Gothenburg, October 2017

Contents

List of Figures

List of Tables

1

Introduction

1.1 Background

In recent years, it has witnessed a revolution in automobile industry-moving towards fully autonomous vehicles. Since the concept of self-sufficient car appeared in 1980s, relevant research and investigation have been boosted significantly. Among all its benefits, the enhanced safety and mobility performance win the praise. The realization of the autonomous cars heavily relies on cooperation of different complicated sub-systems such as sensors, control units, etc. Luckily, the developments in both hardware manufacture and algorithm design can bring them to the reality.

Sensors can be regarded as the 'eyes' of the autonomous cars, being one of the most important parts because they are able to 'see' the surroundings of the moving vehicle and help the vehicle's computer to make more accurate decisions. Thus, various sensors, including radars, cameras, lidars and ultrasonic sensors should work together. Among all these sensors, radar has the most reliable performance in terms of range and velocity detection capability under extreme weather conditions while having moderate cost. Recent developed vehicles tend to have multiple radars for adaptive cruise control, collision avoidance and target classification. Accordingly, the study of characteristics of vehicular radar and the analysis of radar signature are vital for the success of driveless cars.

There are many parameters needed to be studied in a radar system. Different combinations of these parameters have perspectively specific applications. Therefore, the simulations are of great importance to study the effect of those parameters. In order to simulate traffic scenarios, traffic objects need to be characterized accurately from different aspects. For the radars operating at millimeter-wave(mmWave), characterizing and simulating the electromagnetic properties of traffic objects is challenging. As a result, target signatures should be optimized in a computationally efficient way for the convenience of further process.

Some relevant work has been done in this area. Andersson *et al.*, Randolph Moses and Frank Natterer have shown the generation of radar target signature by Fourier reconstruction [1]. Caner Ozdemir implements the four nearest-neighboring interpolation and CLEAN algorithm to have a sparse representation of the target signature [2]. Meta *et al.*, Hoogeboom *et al.* and Leo P. Ligthart show the radar imaging method by Range-Doppler radar and put forward a method to correct phase nonlinearity [4]. The authors in [8] put forward the min-max interpolator for reconstruction.

1.2 Aim

This thesis is aimed to model the traffic object with milimeter-wave and optimize the target signature. Three steps are implemented to realize the goal: investigating Fourier reconstruction methods, sparse representation and processing the real measurement. MATLAB is used in both early stage simulation and measurement process. The entire measurements are performed by RISE Research Institutes of Sweden AB, SP Elektronik with 77 GHz radar.

1.3 Method

The project starts from the model which is generated by manually defining the scattering points. Then, Fourier reconstruction methods and nonlinear optimization are implemented based on this model.

Literature study comes firstly. After comparing different algorithms in terms of computation complexity and reconstruction accuracy, Gridding Method and Unequally Spaced Fourier Transform [1] are implemented. For sparse representation, l_1 optimization with soft thresholding is considered as a good choice in this thesis.

After verifying the algorithms, measurements as well as the artificial data simulated by electromagnetic(EM) simulation tools are processed. We slightly modify the algorithm, because of the difference of scenario in simulation and spot test. Fig.1.1 shows the scheme of the work to accomplish the aim of this thesis.

1.4 Limitations

In this thesis, Fourier reconstruction methods are used to generate radar imaging. The bandwidth of the signal transmitted from the radar directly affects the performance of radar imaging. For example, the radar signature of a point source will not be a point. Instead, it has a point spread function caused by the limited frequency bandwidth. Fig.1.2 and 1.3 show it.

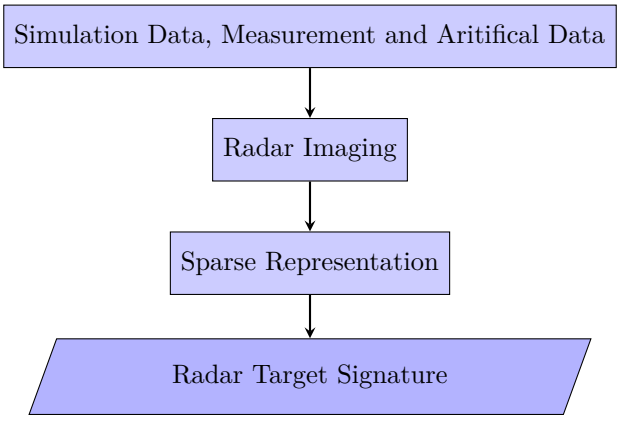

Figure 1.1: Scheme of the thesis.

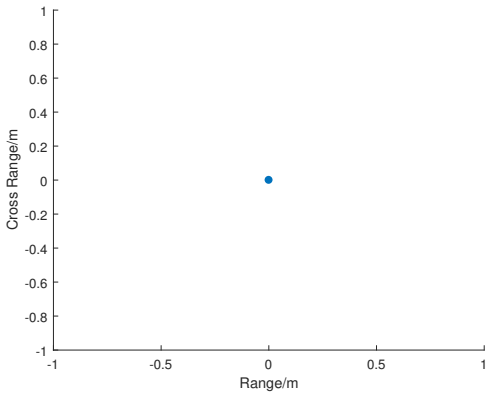

Figure 1.2: Point target

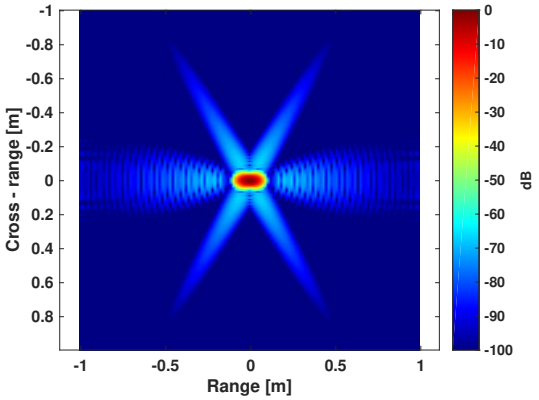

Figure 1.3: Radar signature of the point target.

It's assumed that the frequency and angle information are sampled uniformly. However, in real case this assumption cannot be achieved. So there will be reconstruction errors in final results.

The sparse representation of the radar target signature requires redundant computation. Considering both the hardware condition and project requirements, the performance of the algorithm of sparse representation has to be degraded to some extend.

1.5 Outline of the thesis

In chapter 1, the background of the work, as well as our aim, methods, and limitations are presented. Chapter 2 contains the description of the priori knowledge and theories needed in this work including electromagnetic field, Synthetic Aperture Radar(SAR), Inverse Synthetic Aperture Radar(ISAR) and sparse representation. In the third chapter, Gridding Method and Unequally Spaced Fourier Transform as well as l_1 minimization are implemented to process both real measurements and artificial data. In the final chapter, the comparison of these two algorithm in terms of accuracy and speed, discussion of results and future work are discussed.

2

Theory

2.1 Electromagnetic Scattering

When an Electromagnetic (EM) wave hits an object or target, a physical phenomenon happens which is called scattering. When radiation is only scattered by one localized scattering center, this is called single scattering. It is also very common that scattering centers are grouped together. In such cases, radiation could scatter many times, being known as multiple scattering. Both the wavelength of the EM wave and the shape of the object will determine the way radar signals scatter ([20]).

Raleigh scattering occurs when the size of the scatterer is much smaller than the wavelength of the EM wave, for example, S-band radar waves are scattered by raindrops. When the size of the scatterer is much larger than the wavelength of the EM wave, the scattering is called Mie scattering, similar to the light being scattered by small water droplets in clouds. In [2], some examples regarding different EM wavelengths have been illustrated.

Scattering types can also be classified depending on the wave's trajectory from different structures or shapes that may have flat and smooth surfaces, curved surfaces, edges, or corners. And of course the material of the object also have not negligible effect on scattering.

EM scattering is the key inspiration for radar imaging which just the scattered energy from a target. Scattering centers are just a bunch of localized energy points that compose the radar image.

2.2 Radar Cross Section (RCS)

Radar Cross Section (RCS) can be used to describe how detectable an object is with a radar. The larger the RCS, the more easily the target is detected. The unit of RCS parameter is square-meters. Generally, an RCS parameter is used to categorize the target's EM reflectivity or ability to intercept and re-radiate the EM energy for a particular direction at a particular frequency.

RCS is the main parameter used to detect aircrafts, ships, vehicles or more commonly, military targets. The less observable targets are designed with lower RCS values so that they cannot be detected by the opponent's radar. The research of RCS plays an important role in radar imaging. Actually, inverse synthetic aperture radar (ISAR) images of a target are constructed by backscattered RCS measurements. Then with the backscattered RCS measurements from the target with different frequencies and different look angles, the ISAR image of the target is obtained.

2.2.1 RCS formulation

Briefly, RCS can be described as the effective echoing area of the target when it is illuminated by a plane wave. It can also be regarded as a measure of the ability of an object to scatter EM signals in the direction of the radar receiver. According to the IEEE Standard Definitions of Terms, it is defined as:" For a given scatter, upon which a plane wave is incident, that portion of the scattering cross section (SCS) corresponding to a specified polarization component of the scattered wave" ([21]). A more formal definition of RCS of an object is the amount of power of the intercepted equivalent area that, when scattered isotropically, produces a power density at the radar receiver that is equal to the density scattered by the actual object ([22]).

The formula of RCS can be derived as in the following: Assume that the object is located at distance R from the radar, and the incident plane wave from the radar transmitter produces a power density of W^i at the target. If the target has a RCS area denoted by σ, then the power reflected by the target is ([2])

$$P_r = \sigma \cdot W^{\mathrm{i}} \tag{2.1}$$

which will be re-radiated in all directions. Therefore, the power density W^s of the reflected wave at the radar receiver is

$$W^{\mathrm{s}} = \frac{P_r}{4\pi R^2}. \tag{2.2}$$

Hence the formal equation of RCS is easily obtained as follows

$$\sigma = 4\pi R^2 \frac{W^{\mathrm{s}}}{W^{\mathrm{i}}}. \tag{2.3}$$

When the incident EM wave hits the target, the scattered energy will radiate in all directions; Only the scattered energy in the direction of radar receiver is counted in the RCS caculation. If the radar transmitter and receiver are collocated, then the energy collected by the radar is called backscattered energy. If the radar receiver, however, is located in a different place from transmitter, then the calculated cross section will provide bistatic RCS.

2.3 Radar Waveforms

Both different applications of the radar and specific role will decide what kind of radar signal type we will choose. Therefore, different waveforms of radar can be utilized for the various radar applications.In this thesis project, we utilize FMCW reference radar. The most commonly used radar waveforms are ([3],[23]):

- Continuous wave (CW)
- Frequency modulated continuous wave (FMCW)
- Stepped frequency continuous wave (SFCW)
- Linear frequency modulated pulse (LFM)

2.3.1 Continuous wave (CW)

The time-domain signal of the CW radar can be written simply as

$$s(t) = A \cdot cos(2\pi f_0 t), \tag{2.4}$$

where f_0 is the operating frequency. The frequency spectrum of this CW signal can be found by applying Fourier transform operation to (2.4) to get

$$S(f) = \frac{A}{2} \cdot (\delta(f - f_0) + \delta(f + f_0)). \tag{2.5}$$

A CW radar system transmits radio wave signals at a particular frequency f_0. If both the radar and the target are stationary, then the frequency of the received signal stays unchanged. On the other hand, if the target is moving with respect to the radar, the returned signal's frequency components are shifted from transmitted frequency f_0, which is called Doppler effect and the shift in freq. is Doppler shift ([23]). and plays an important role in finding the velocity of the target in most radar applications.

2.3.2 Frequency modulated continuous wave (FMCW)

The CW radar can only estimate the Doppler shift caused because of the movement of the target with respect to radar, but FMCW radar can be used to determine the range of the target, as shown in [3]. The most common way to modulate the frequency is simply increasing the frequency as the time passes, which is also known as linear frequency modulation or chirp modulation.

In [3], the waveform of an LFM continuous wave signal is given by

$$s(t) = A \cdot sin(2\pi(f_0 \mp \frac{K}{2}t)t), \tag{2.6}$$

where A is the signal amplitude, f_0 is the starting frequency, and K is the chirp rate (i.e., the frequency changing rate), and the "+" sign indicates an up-chirp signal and the "−" sign indicates a down-chirp signal. Fig. 2.1 shows a simple up-chirp signal in time domain for which the frequency of the wave increases with time.

In FMCW radar systems, consecutive LFM signals are transmitted with the period T, then the received signal arrives with a time delay of t_d which is related to the range of the target and can be determined by the difference in the frequency between the transmitted and the received signals Δf:

$$\Delta f = f_\mathrm{tx} - f_\mathrm{rx} = \mp K \cdot t_\mathrm{d}, \tag{2.7}$$

where $t_\mathrm{d} = \frac{2R}{c}$, and c is the speed of light in the air.

2.3.3 Stepped frequency continuous wave (SFCW)

The Step Frequency Wave Radar (SFCW) is another well-known radar technology which has two main advantages compared to above-mentioned technologies: [19]

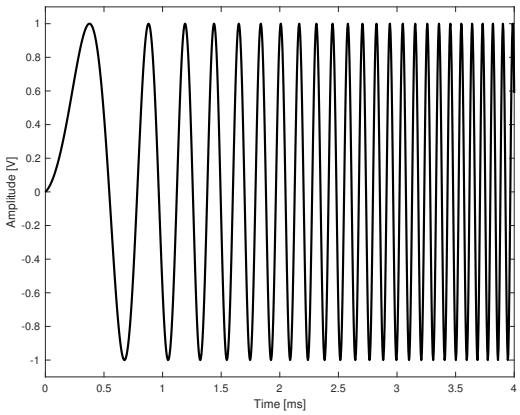

Figure 2.1: A linear frequency modulated continuous wave signal (upchirp) (here $f_0 = 100, K = 3 \cdot 10^6$)

[1]. The signal is formed by emitting a series of single-frequency short continuous waveforms, formulated by $f_n = f_0 + (n-1) \cdot \Delta f$, where Δf is an incremental frequency.

The SFCW signal can also be used to estimate the range of a possible target. Assume that the target is at the range distance of R_0 from the radar, then the phase of the backscattered wave is exponentially related to the range as in the following

$$E^s[f] = A \cdot \mathrm{e}^{-\mathrm{j}2k \cdot R_0}, \tag{2.8}$$

where E^s is the scattered electric field, A is the amplitude, and k is the wavenumber vector. One can establish the Fourier Transform relationship between $(2k)$ and (R), so that the range R_0 can be resolved by taking the inverse Fourier transform of the output of the SFCW radar, as shown in Fig.2.2.

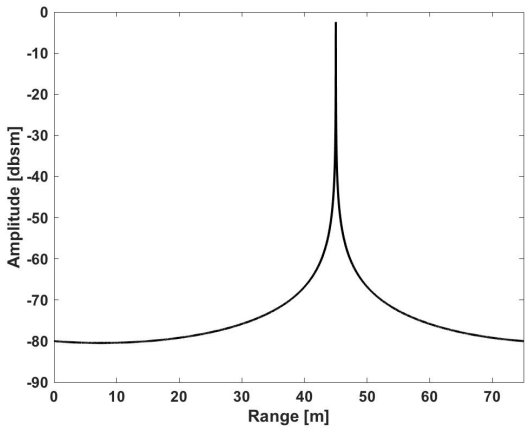

Figure 2.2: Range profile of a point target (45m) is obtained by SFCW radar

[1]introduced more details about how SFCW radar fulfills range detection

2.3.4 Linear frequency modulated pulse (LFM)

Another common waveform is the Linear Frequency Continuous wave (LFM) pulse, also known as the chirp pulse, shown in Fig.2.3. Here it is an upward chirp signal whose frequency is increasing with rate k.

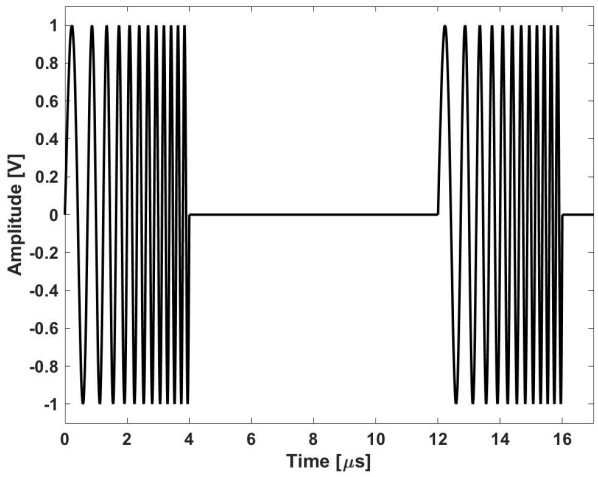

Figure 2.3: LFM pulse (chirp)
($f_0 = 10^6, k = 10^{12}, T_{PRI} = 4\mu s$)

In general, this waverform is repeated in every interval of duration T_{PRI} intervals for most common radar applications, especially for localization of targets. T_{PRI} is called Pulse Repetition Interval (PRI).

2.4 Radar Imaging

Traditional application of radar is the detection of position or motion of the reflective object by analyzing the time delay or Doppler shift of the echo from a specific direction. Radar imaging is capable of forming an image by illuminating the reflective object and mapping the intensity of reflected signals onto a two-dimensional plane. The intensity is determined by the amount of scattering of the target, thus a two-dimensional description of the object can be given.

2.4.1 Inverse Synthetic Aperture Radar Imaging

Inverse Synthetic Aperture Radar (ISAR) is a strong signal processing technique for imaging stationary targets in range and cross-range domains. Range implies the direction of propagation from radar toward the target, cross-range is defined as the perpendicular axis to the range direction. An ISAR image has the ability to display the dominant (stronger) scattering regions which are so called scattering centers on the target. It is normally implemented for identification and classification of targets.

ISAR is utilized in many applications specially when the motion of the object often plays a more important role than the rotation, e.g., in maritime surveillance

for the classification of ships and other objects or in autonomous driving for the recognition of vehicles.

Now we need to consider about how the scattered field or the reflectivity function from a target can be related to the ISAR imaging function of the target. As known in [2], the scattered electric field from any object is shown to be equal to

$$\mathbf{E}^{\mathrm{s}}(\mathbf{r}) = -\frac{\mathrm{j}k_0 E_0}{4\pi r}\mathrm{e}^{-\mathrm{j}k_0 r}\iint_{S_{lit}} 2\hat{n}(\mathbf{r}') \times (\hat{\mathbf{k}}^i \times \hat{\mathbf{u}})\mathrm{e}^{\mathrm{j}(\mathbf{k^s}-\mathbf{k^i})\cdot\mathbf{r}'}d^2\mathbf{r}', \tag{2.9}$$

assuming the perfect conducting. Table 2.1 shows what the parameters indicate in (2.9).

Table 2.1: Parameters

$\mathbf{k}^s$,$\mathbf{k}^i$	incident and scattered wavenumber vectors
$\hat{\mathbf{n}}(\mathbf{r}')$	outward surface unitary normal vector
$\hat{\mathbf{k}^{\mathbf{i}}}$	unit vector in incident wave direction
E_0	magnitude unit vector of the incident wave
$\hat{\mathbf{u}}$	polarization unit vector of the incident wave
S_{lit}	illuminated part of the object's surface

Now if we assume that the receiving antenna has a particular polarization which collects the scattered field in the $\hat{v}$ direction, then rewrite (2.9) as

$$\hat{\mathbf{v}} \cdot \mathbf{E}^{\mathrm{s}}(\mathbf{r}) = -\frac{\mathrm{j}k_0 E_0}{4\pi r}\mathrm{e}^{-\mathrm{j}k_0 r}\iiint_{-\infty}^{\infty} O(\mathbf{r}')\mathrm{e}^{\mathrm{j}(\mathbf{k^s}-\mathbf{k^i})\cdot\mathbf{r}'}d^3\mathbf{r}', \tag{2.10}$$

where $O(\mathbf{r}') = \hat{\mathbf{v}} \cdot [2\hat{\mathbf{n}}(\mathbf{r}') \times (\hat{\mathbf{k}}^i \times \hat{\mathbf{u}})] \cdot \delta(S(\mathbf{r}'))$ is called scalar Object Shape Function (OSF). And $S(\mathbf{r}') = \begin{cases} \neq 0 & \mathbf{r}' \in S_{lit} \\ 0 & \mathbf{r}' \in S_{shadow} \end{cases}$.

Then if we define the 3D Fourier transform of the OSF $O(\mathbf{r}')$ as

$$\tilde{O}(\mathbf{k}) = \iiint_{-\infty}^{\infty} O(\mathbf{r}')\mathrm{e}^{\mathrm{j}(\mathbf{k^s}-\mathbf{k^i})\cdot\mathbf{r}'}d^3\mathbf{r}', \tag{2.11}$$

then rewrite the scattered electric field in the $\hat{\mathbf{v}}$ direction

$$\hat{\mathbf{v}} \cdot \mathbf{E}^{\mathrm{s}}(\mathbf{r}) = (-\frac{\mathrm{j}k_0 E_0}{4\pi r}\mathrm{e}^{-\mathrm{j}k_0 r})\tilde{O}(\mathbf{k}^{\mathrm{s}} - \mathbf{k}^{\mathrm{i}}). \tag{2.12}$$

(2.12) gives the scattered field along the $\hat{\mathbf{v}}$ direction, and clearly shows that the scattered electric field from a target is proportional to 3D FT of its OSF. In other words an SAR image can be seen as the display of this OSF onto the 2D or 3D plane. Moreover it is also obvious to notice that OSF varies with respect to the look angle and the frequency of practical operation.

2.4.2 SAR versus ISAR

Inverse sythentic aperture radar (ISAR) is a high-resolution airborne and space-borne remote sensing technique for imaging remote targets. ISAR has been primarily utilized for surveillance applications such as detection of opponents' territories,

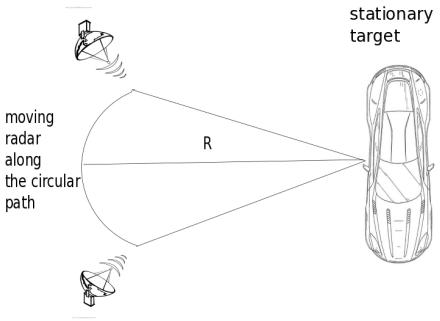

Figure 2.4: Spotlight SAR with circular vehicle path

airplanes, tanks and buildings, but it has also found many real-world applications ranging from geophysics to archeology. ISAR also can provide fine resolutions both in range and cross-range dimensions.

Generally ISAR refers to the case where the radar platform is moving while the target stays stationary, as shown in Fig. 2.4. On the other hand, the term SAR is used for scenarios when the radar is stationary and the targets are in motion, as illustrated in Fig. 2.5.

2.4.3 Range Profile

As mentioned before, ISAR image can be regraded as the display of range and cross-range profiles of the target in 2D plane. In this section, we focus on the understanding of the meaning of the range profile. A range profile is the returned waveform from illuminated by radar with certain frequency bandwidth from the target, as shown in Fig.2.6. When the illuminating wave wave is a time-domain pulse, then the reflected signal from the target collected by the receiver would have 1D characteristics, typically field intensity versus time, as shown in Fig.2.7. On the other hand, if the illuminating signal is the stepped frequency waveform, the the IFT of the received signal characterizes the 1D range profile of the target.

Fig.2.6 also shows the physical meaning of the range profile, where the vehicle is the target. As the incident wave passes along with the target (vehicle), some of the energy reflects back toward the radar from scattering centers on the target, which are located at different range distances from the radar. Then they will return at different time instants to the receiver so that they can be distinguished in the corresponding 1D range profile. But, it is impossible to resolve the scattering centers being in the same range i.e.,located at the same distances to the radar, therefore cross-range in this case may help.

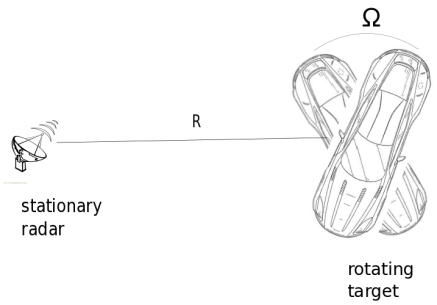

Figure 2.5: ISAR

Generally, the range profile is displayed versus distance (range), instead of time, since it is more meaningful physically. So, the range axis can be scalded as

$$r = \mathrm{c} \cdot t, \tag{2.13}$$

where r is range, c is the speed of light and t is time.

Now let us show how we can obtain range profile by processing the returned wave with various frequency. Assume there are N point scatterers along the range-axis (x-axis) each located at a different x_i location. Then, according to [2] the backscattered electric field at the far-field can be approximated as

$$\begin{aligned} E^{\mathrm{s}}(f) &\cong \sum_{i=1}^{N} A_i \mathrm{e}^{-\mathrm{j}2kx_i} \\ &= \sum_{i=1}^{N} A_i \mathrm{e}^{-\mathrm{j}2\pi(\frac{2f}{c})x_i}, \end{aligned} \tag{2.14}$$

where A_i is the backescattered field amplidtude for the point scatterer at x_i and $k = \frac{2\pi f}{\mathrm{c}}$ is the corresponding wave number for frequency f. The scaler "2" is because of two way propagation between radar and the point scatterers. Then the range profile can be constructed by inverse Fourier transforming $E^{\mathrm{s}}(f)$ with respect to

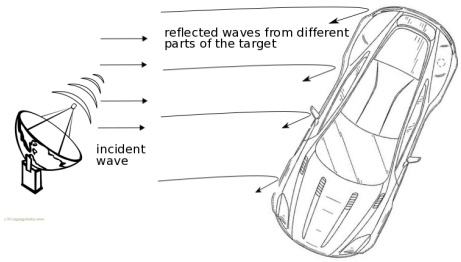

Figure 2.6: Physical meaning of range profile

$(\frac{2f}{\mathrm{c}})$ as given below:

$$\begin{aligned} E^{\mathrm{s}}(x) &= F^{-1}\{E^{\mathrm{s}}(f)\} \\ &= \int_{-\infty}^{\infty} [\sum_{i=1}^{N} A_i \mathrm{e}^{-\mathrm{j}2\pi(\frac{2f}{\mathrm{c}})x_i}] \mathrm{e}^{j2\pi\frac{2f}{\mathrm{c}}x} d(\frac{2f}{c}) \\ &= \sum_{i=1}^{N} A_i \int_{-\infty}^{\infty} \mathrm{e}^{-\mathrm{j}2\pi(\frac{2f}{\mathrm{c}})(x-x_i)} d(\frac{2f}{\mathrm{c}}) \\ &= \sum_{i=1}^{N} A_i \delta(x - x_i). \end{aligned} \tag{2.15}$$

Now $E^s(x)$ represents the range profile as a function of range x, which indicates the point scatterers located at different x_i locations are pinpointed in the range axis with their corresponding backscattered field amplitudes A_i.

However, the point to be considered is that the result in (2.15) is valid for the infinite bandwidth. In reality, it is impossible to collect data within a infinite bandwidth of frequencies. Now considering the frequency range from $\mathrm{f_L}$ to $\mathrm{f_H}$, one can rewrite the eq2.15 with defining the center frequency $f_c = \frac{\mathrm{f_L}+\mathrm{f_H}}{2}$ and corresponding wave number $k_c = \frac{2\pi f_c}{c}$ and bandwidth $\mathrm{B} = \mathrm{f_H} - \mathrm{f_L}$ as below

$$\begin{aligned} E^{\mathrm{s}}(x) &= \sum_{i=1}^{N} A_i \int_{f_L}^{f_H} \mathrm{e}^{-\mathrm{j}2\pi(\frac{2f}{\mathrm{c}})(x-x_i)} d(\frac{2f}{c}) \\ &= (\frac{2\mathrm{B}}{c}) \sum_{i=1}^{N} A_i \mathrm{e}^{\mathrm{j}2k_c(x-x_i)} sinc(\frac{2\mathrm{B}}{c}(x - x_i)). \end{aligned} \tag{2.16}$$

It is unavoidable that *sinc* defocusing around the scattering centers in the range profile pattern due to finite bandwidth of the radar signal, which is also known as Point Spread Function (PSF) in the radar literature.

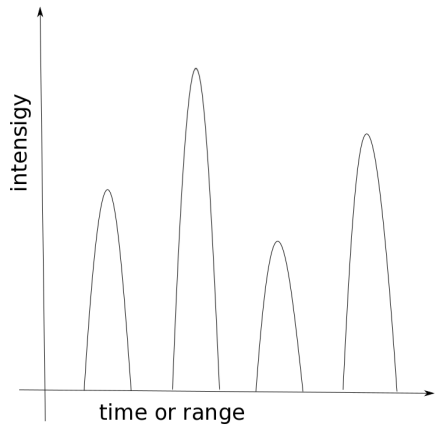

Figure 2.7: Range profile of a target

If the frequency bandwidth is B, then the resolution in range Δx is

$$\Delta x = \frac{c}{2\mathrm{B}}. \tag{2.17}$$

Then the total viewed range or range extend X_{max} is

$$X_{max} = N \cdot \Delta x = \frac{N \cdot c}{2\mathrm{B}}. \tag{2.18}$$

X_{max} should be greater than the length of the target in the range to avoid any ambiguity that may cause aliasing.

Range profile plays a great role in radar imaging. It can be used as a common tool for extracting the scattering centers and also for determining the length of a target.

2.4.4 Cross-Range Profile

Similar obtaining the range profile, a cross-range profile can also be formed by collecting the radar returns from a target at different look angles, as shown in Fig.2.8. While the range profile is obtained by treating the backscattered field at single look angle but different frequencies, the cross-range profile is acquired by processing the backscattered field at one frequency but different look angles. Assume P scattering points located at different positions (x_i, y_i). Then the backscattered electric field at

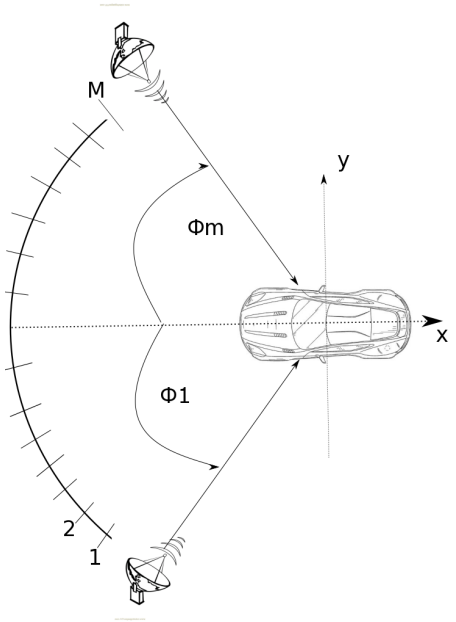

Figure 2.8: Collecting radar returns at different look angles to form the cross-range of a target

the far field for different angles can be approximated as

$$\begin{aligned} E^{\mathrm{s}}(\Phi) &= \sum_{i=1}^{P} A_i \mathrm{e}^{-\mathrm{j}2\mathbf{k}\mathbf{r}_i} \\ &= \sum_{i=1}^{P} A_i \mathrm{e}^{-\mathrm{j}2k\cos\Phi x_i} \mathrm{e}^{-\mathrm{j}2k\sin\Phi y_i} \\ &= \sum_{i=1}^{P} B_i \mathrm{e}^{-\mathrm{j}2k\Phi y_i} \\ &= \sum_{i=1}^{P} B_i \mathrm{e}^{-\mathrm{j}2(\frac{2f}{c})\Phi y_i}, \end{aligned} \tag{2.19}$$

where r_i is the vector from the origin to the point scatterer at (x_i, y_i) and A_i is the backscattered field amplitude for corresponding point scatter. For small look angle Φ, we approximated $cos\Phi$ as 1 and $sin\Phi$ as Φ.

Then do 1D IFT of (2.19) with respect to $\frac{2f}{c}\Phi$ which can resolve y_i in the cross range, as shown below

$$\begin{aligned} E^{\mathrm{s}}(y) &= \mathcal{F}^{-1}\{E^{\mathrm{s}}(\Phi)\} \\ &= \sum_{i=1}^{P} B_i \delta(y - y_i). \end{aligned} \tag{2.20}$$

Here $E^s(y)$ represents the cross range funtion as a function of y. The point scatterers located at different cross-range locations y_i is perfectly pinpointed in the cross-range axis. Of course, the result in (2.20) is valid when we collect the backscattered field data from infinite numbers of look angles. So in reality, rewrite (2.20) similarly

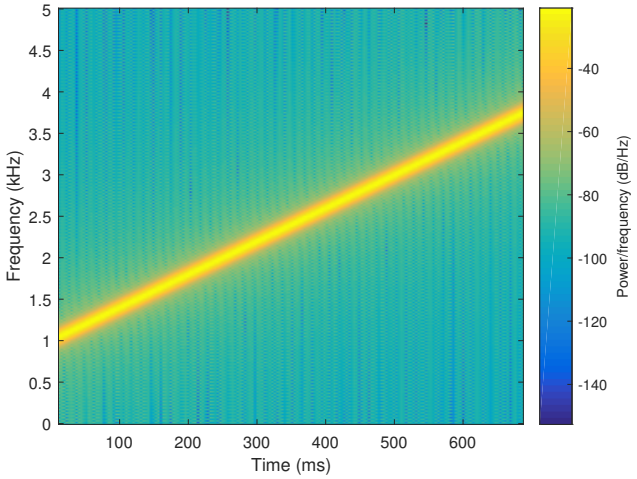

Figure 2.9: How VCO works.

as what we did to get range profile

$$E^{s}(y) = (\frac{2f}{c}\Omega)\sum_{i=1}^{P} B_i sinc(\frac{2f}{c}\Omega(y - y_i)). \tag{2.21}$$

2.4.5 Radar Model

The radar signal is generated by using the Voltage Controlled Oscillator(VCO). The frequency of the signal changes linearly with voltage on VCO. Fig. 2.9 shows the frequency as a function of time. For FMCW radar with dual channels, the transmitted signal has the complex waveform shown below:

$$s(t) = A \cdot e^{j2\pi(f_0 t + \frac{K}{2}t^2)}. \tag{2.22}$$

Assume there are N_t targets illuminated by the radar wave with positive chirp rate, then the return signal has the following form:

$$s_r(t) = \sum_i A_i \cdot e^{j2\pi(f_0(t-\tau_i) + \frac{K}{2}(t-\tau_i)^2)}, \tag{2.23}$$

where τ_i's represent the time delay caused by the target. Then the return signals are multiplied with the conjugate of the transmitted signal with a low-pass filter to realize down-chirp, then the output from the radar would be:

$$s_o(t) = \sum_i A_i \cdot e^{j2\pi f \tau_i} = \sum_i A_i \cdot e^{j2\pi f \frac{2R_i}{c}} = \sum_i A_i \cdot e^{j2kR_i} = \sum_i A_i \cdot e^{j\xi R_i}, \tag{2.24}$$

where R_i's show the distance of the targets. This is for the 1D case. If the radar scans different angles, and the output is shown in (2.25).

2.4.6 Format 2D SAR image

In practice, the SAR image is produced by collecting echoed data set from a small frequency bandwidth of B and a small angle Ω. Also in this section, we only consider

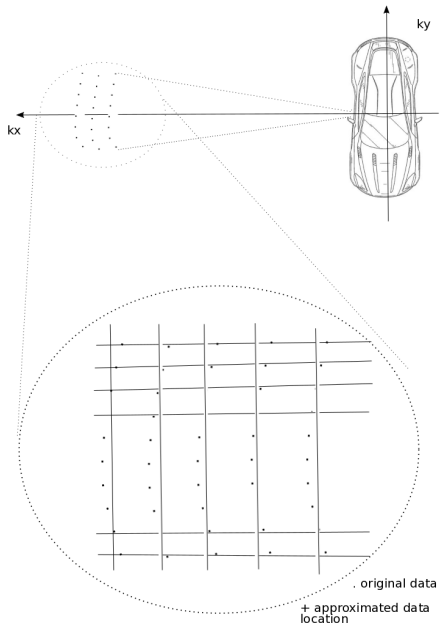

Figure 2.10: SAR data collection for small bandwith and angle on $k_x - k_y$ plane

monostatic SAR (which the transmitter and the receiver are positioned in the same place).

Actually the 2D SAR image is just the display of range profile in one axis and the cross-range profile in the other axis, but the scattered data should be collected from various frequencies and look angles. Fig.2.10 shows the 2D SAR image lie on the 2D $k_x - k_y$ plane, since we only consider the backscattered electric field data are collected within a sufficiently small bandwidth and look angle. In Fig.2.10 ,the data grid in $k_x - k_y$ space approaches to equally spaced linear grid which paves the way to use inverse fourier transform.

In order to get the algorithm for 2D SAR image, let us start with a scenario where a point scatterer $P(x_0, y_0)$ located at azimuth angle Φ, then according to [2] the backscattered field can be approximated as

$$E^s(k, \Phi) \cong A_0 \cdot \mathrm{e}^{-\mathrm{j}2\mathbf{kr}_0}, \tag{2.25}$$

where A_0 is the amplitude, $\mathbf{k}$ is the vector wave number in the propogation direction, and $\mathbf{r}_0$ is the vector from origin to point P. In small-bandwidth small-angle ISAR imaging, the frequency bandwidth B is small compared to center frequency f_c, then the wave number k in the second phase term can be approximated as

$$k \cong k_c = \frac{2\pi f_c}{\mathrm{c}}. \tag{2.26}$$

Similarly, if the look angel Φ is small, we can do the approximation like below

$$\begin{aligned} cos\Phi &\cong 1 \\ sin\Phi &\cong \Phi \end{aligned} \tag{2.27}$$

In practice, when the bandwidth is less than one-tenth of the center frequency, it is considered as sufficiently small. Angular widths are also considered as sufficiently

small if they are at most 5° to 6°, then according to the above approximations, one can rewrite the backscattered electric field from point P

$$\begin{aligned} E^{\mathrm{s}}(k,\Phi) &= A_0 \cdot \mathrm{e}^{-\mathrm{j}2k\cdot x_0} \cdot \mathrm{e}^{-\mathrm{j}2k_c\Phi y_0} \\ &= A_0 \cdot \mathrm{e}^{-\mathrm{j}2\pi\frac{2f}{c}x_0} \cdot \mathrm{e}^{-\mathrm{j}2\pi\frac{k_c\Phi}{\pi}y_0}. \end{aligned} \tag{2.28}$$

In the similar manner, we obtain the SAR image in the $x-y$ plane by taking the 2D IFT of (2.28) as

$$\begin{aligned} E^{\mathrm{s}}(x,y) &= \mathcal{F}_2^{-1}\{E^{\mathrm{s}}(k,\Phi)\} \\ &= A_0 \cdot \mathcal{F}_1^{-1}\{\mathrm{e}^{-\mathrm{j}2\pi\frac{2f}{c}x_0}\} \cdot \mathcal{F}_1^{-1}\{\mathrm{e}^{-\mathrm{j}2\pi\frac{k_c\Phi}{\pi}y_0}\} \\ &= A_0 \cdot \delta(x-x_0, y-y_0) \\ &\triangleq SAR(x,y). \end{aligned} \tag{2.29}$$

The backscattered electric field from a target can be approximated as the sum of finite single scattering points.If we assume there are M scattering centers in total, then

$$SAR(x,y) = \sum_{i=1}^{M} A_i \cdot \delta(x-x_i, y-y_i). \tag{2.30}$$

In more general cases, the backscattered data are collected within a wide angle range. Also, according to (2.17), in order to achieve higher resolution in SAR imaging, the bandwidth of transmitted signal should be reasonably large. So the above-mentioned assumptions made above do not exist and the collected SAR data cannot be regarded as uniformly distributed. Thus direct application of Fourier transform of the backscattered data will be incorrect.

For wide angle and wide bandwidth, the measurement $E^{\mathrm{s}}(k,\Phi) = E^{\mathrm{s}}(\xi_s)$ has the support on

$$\xi_s = \left\{ \left[\frac{4\pi f}{c} cos(\Phi), \frac{4\pi f}{c} sin(\Phi) \right] : f_{min} \le f \le f_{max}, |\phi| \le \Phi \right\}. \tag{2.31}$$

The index s represents the sampling geometry. In our thesis, the sampling geometry is circular sampling and s can be written as $s = \left[i, l\right]^{\mathsf{T}}$ where i and l represent the number of frequency and angle samples.

Interpolation should be applied to these data before Fourier transform and there are many interpolaters to modify the backscattered data. Details will be discussed in next chapter.

2.5 Sparse Representation

2.5.1 Sparse Representation

Sparse representations of signals have been of great attention and importance in image processing [13] [2], biology, document analysis, and audio analysis for representation, compression, and estimation etc. The problem is solved by optimizing an

[2] explains how compressive sensing works for radar image processing

objective function which has two terms: one that measures the signal reconstruction error and the other measureing the sparsity, searching for the sparse representation of a signal over an overcomplete dictionary in terms of linear combination of atoms.

2.5.2 l_p norm

In mathematics, the l_p spaces are function spaces defined using a natural generalization of the $p-norm$ for finite-dimensioal vector spaces. For a real number $p > 1$, the $p-norm$ of x is defined by ([24])

$$\| x \|_p = (| x_1 |^p + | x_2 |^p + \cdots + | x_n |^p)^{\frac{1}{p}}. \tag{2.32}$$

$l_1 - norm$ is also known as the least absolute deviations (LAD) and the least absolute errors (LAE). It is aiming at minimizing the sum of the absolute differences between the target value (y_i) and the estimated values ($f(x_i)$).

$$\min \sum_{i=1}^{n} | y_i - f(x_i) | . \tag{2.33}$$

$l_2 - norm$ is also known as least suqres. It is aiming at minimizing the sum of the square of the differences between the target value and the estimated values.

$$\min \sum_{i=1}^{n} (y_i - f(x_i))^2. \tag{2.34}$$

$l_2 - norm$ always has one solution but it is non-sparse outputs.

$l_1 - norm$ sometimes has multiple solutions but they are sparse outputs. In our case, we implement $l1 - norm$ minimization to fulfill sparse representation of our radar image.

2.5.3 Sparse Representation of signal

Finding the sparse representation of a signal given an overcomplete dictionary by considering the problem [16]

$$\min \| y - Ax \|_2^2 + \mu \| x \|_1. \tag{2.35}$$

where $\mathbf{A} \in \mathbb{R}^{N \times M}$ containing the elements of an overcomplete dictionary in its columns, with $M > N$, named as sensing matrix, and $\| x \|_1$ is l_1 norm. And a signal $y \in \mathbb{R}^N$ is the signal which needs to be represented sparsely by x. Now the problem of sparse representation is to find an $M \times 1$ coeffcient vector x, which satisfies equation 2.35. (2.35) has two parts: reconstruction error and sparsity. Term μ is a scalar regularization parameter that balances the trade-off between these two parts.

3

Methods and Results

3.1 Gridding Method

As we mentioned in previous chapter, the assumption of backscattered data does not hold if radar operates within wide angles and wide bandwidths. In this case, the data is distributed on uniform polar grid and directly applying FFT would cause reconstruction errors. Thus, proper interpolation of the data is necessary.

Gridding Method (GM) is a classic method which has been widely used for medical image reconstruction [2]. It approximates the inverse Fourier transform integral in (2.25) by applying a weight function to backscattered data. Compared to the conventional Polar Format Algorithm [2], Gridding Method is more computationally expensive. However, it provides two benefits. First, Polar Format Algorithm may fail if the range of look angle is too large while Gridding Method can handle azimuth range even for full circle [1]. Second, there exists user-control parameters to make a trade-off between computational complexity and reconstruction error.

The core of the Gridding Method is the use of a weight function W(x):

$$\mathrm{W}(x) = \Big\{ [x_1, x_2]^\intercal : |x_1| \leq \tilde{R}_1, |x_2| \leq \tilde{R}_2 \Big\}, \tag{3.1}$$

where $\tilde{R}_1$ and $\tilde{R}_2$ are supports of the weight function W(x). The Fourier transform $\tilde{W(\xi)}$ should center at $\xi = 0$, and the interpolation goes:

$$\tilde{\mathrm{W}}(\xi) * \mathrm{E}^s(\xi) = \int \tilde{\mathrm{W}}(\xi - \eta)\mathrm{E}^s(\eta) d\eta. \tag{3.2}$$

According to the trapezoidal rule, the integral can be approximated as:

$$\tilde{W}(\xi) * \mathrm{E}^s(\xi) \approx 4\Delta\phi\Delta k \sum_i k_i \sum_l \tilde{\mathrm{W}}(\xi - \xi_{i,l})\mathrm{E}^s(\xi_{i,l}). \tag{3.3}$$

Assume the support of the target is

$$\mathrm{D} = \Big\{ [x_1, x_2]^\intercal : |x_1| \leq R_1; |x_2| \leq R_2 \Big\}, \tag{3.4}$$

then the step size k has an upper bound [1]

$$\Delta k \leq \frac{\pi}{2(R + \tilde{R})}, \tag{3.5}$$

where $R = \sqrt{R_1^2 + R_2^2}$ and $\tilde{R} = \sqrt{\tilde{R}_1^2 + \tilde{R}_2^2}$.

There are many choices of weight function. A popular choice is Kaiser-Bessel window or Gaussian window. In [1], the modified Kaiser-Bessel window is used while [9] exploits the Gaussian window. In [8], the comparison is made between these two window functions with the conclusion that the modified Kaiser-Bessel window has an advantage in reconstruction error over Gaussian window. In our thesis, modified Kaiser-Bessel window in [1] is used. After the interpolation, inverse Fourier transform is applied to obtain the reconstructed image. The weight function is treated as an interpolator for the backscattered data and its effect is removed after interpolation by factorizing the weight function in time domain.

The modified Kaiser-Bessel window $\mathrm{W}(\mathbf{x}) = \mathrm{W}(x_1)\mathrm{W}(x_2)$ has the form:

$$\mathrm{W}(x_i) = \begin{cases} I_0(A\sqrt{(\tilde{R_i}^2 - \mathrm{x_i}^2)}), & |x_i| \leq \tilde{R_i} \\ 0, & \text{otherwise} \end{cases}, \tag{3.6}$$

with the Fourier transform

$$\tilde{\mathrm{W}}(\xi_i) = 2\frac{\sinh(R_i\sqrt{\tilde{A^2 - \xi_i^2}})}{\sqrt{A^2 - \xi_i^2}}, \tag{3.7}$$

where I_0 is the Bessel function of zero order, and A is a user-control parameter. A good choice of parameters in Gridding Method is given as [1]:

$$\begin{cases} \tilde{R_i} = 2 \cdot R_i \\ A = \frac{9\pi}{2\tilde{R_i}} \\ \Delta\xi_i = \frac{\pi}{\tilde{R_i}} \end{cases}, \tag{3.8}$$

The first and third term in (3.8) imply a oversampling rate of 2, and the selection of A is a trade-off between computation complexity and reconstruction error. The larger value for A make the interpolation more precise, but on the other hand, requires more computation.

3.1.1 Simulation

To verify the algorithm, a model is generated as shown in Fig.3.1. The hollow blue points are scattering points on the vehicle. The radar is assumed to rotate between -30° to 30° with central frequency 8 GHz and 4 GHz bandwidth.

The backscattered signal has discontinuities, so in [1] exploiting an apodizing window to smooth the return signal before interpolation is suggested. The two-dimensional Taylor window with four nearly constant-level side-lobes adjacent to the main-lobe, and a maximum side-lobe level -100 dB smaller than the main-lobe peak. An increase of number of nearly constant-level side-lobes can suppress side-lobe of radar signature, but it degrades the resolution at the same time. Fig.3.3 displays the apodizing window, and Fig.3.4 shows the comparison of the original signal and the signal after smoothing from look-angle -30°. The discontinuities in the beginning and the end of the original signal are eliminated.

Fig.3.5 and 3.6 show the result of interpolation and target signature, respectively. The interpolation figure can be characterized as a sector where the look-angle and

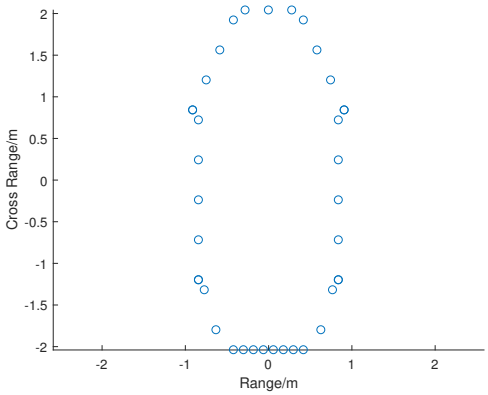

Figure 3.1: Target model.

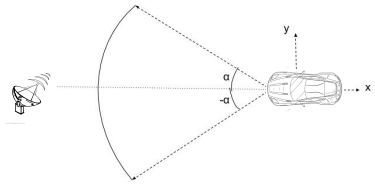

Figure 3.2: Simulation scenario

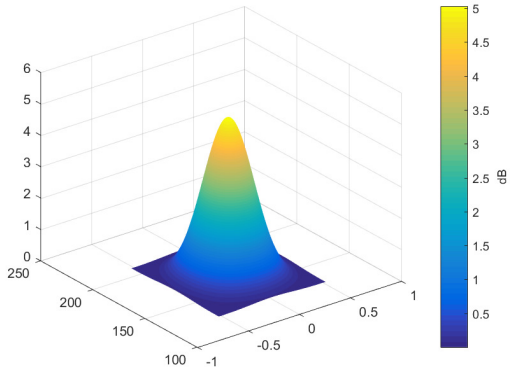

Figure 3.3: Apodizing window.

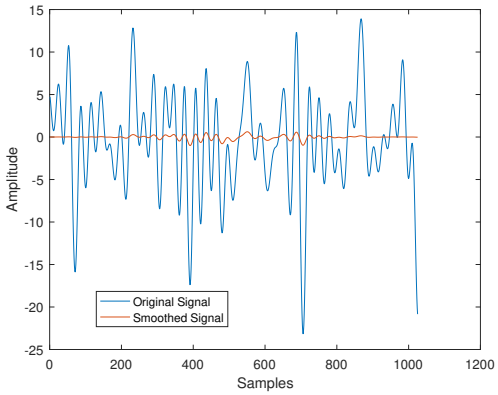

Figure 3.4: Signal comparison

bandwidth of the scenario can be viewed. The target signature has a large dynamic range, and the point spread function in this case can be seen clearly. The target signature is the same as the target model except for those side-lobes caused by limited radar bandwidth.

3.1.2 Measurement

After verifying the Gridding Method, we proceed to handle real measurements. The measurements in this thesis were obtained in the anechoic chamber "Faraday" at RISE in Borås, Sweden. The target is Volvo V40 with 2.041 m width and 4.369 m length, and the distance between radar and rotation center is 14.8 m. The scenario of measurements is shown in Fig.3.7 ,and the parameters are given below:

Table 3.1: Measurement Scenario

Bandwidth(GHz)	1
Central Frequency(GHz)	77
Look-angle(°)	13.66 to 373.66

In previous simulation, the scattering points on target are assumed to be known

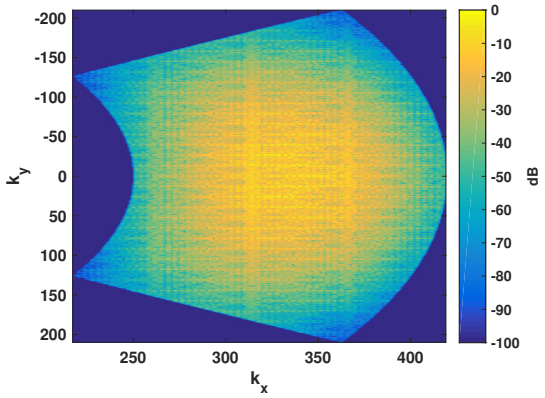

Figure 3.5: The result of interpolation.

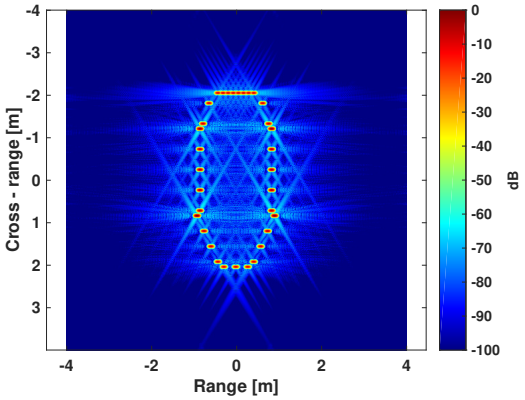

Figure 3.6: Target signature

and the rotation center is exactly the center of the target. However, for measurements, the assumption doesn't hold so determining the rotation center is the priority. Without a correct rotation center, the radar imaging would fail.

The Fourier transform of the backscattered signals is taken to obtain the sinogram, as shown in Fig.3.8. It can be seen that there are a lot of interference in near and far field while the sinogram of the target is located between 10 to 20 meters. Thus, a Tukey window is applied to filter out the interference. Fig.3.9 shows the pure sinogram of the target.

The next step is to find the rotation center, which means the center of rotation should be the center of the sinogram. It's accomplished by either directly cutting the sinogram. Also, calibration is needed to eliminate the background noise. A corner reflector with side 100 mm(14.4 dBsm) is placed at a position which is along the line between the radar and the rotation center. The backscattered signal is treated as a reference signal for calibration. Fig.3.10 shows the modified sinogram with both calibration and rotation center correction. Subsequently, the inverse Fourier transform is applied to obtain the measurement in frequency-angle domain. Fig.3.11 shows it. The difference between the modified measurement and the original one is that the frequency is down-converted to baseband with 1GHz bandwidth. Fig.3.12 illustrates the scenario for calibration.

Fig.3.13 shows the final target signature, Volvo V40. It can be seen that the flanks have much stronger reflectivity than front or tail, which is consistent with the sinogram shown in Fig.3.8. Even though calibration is already done, the background noise is still quite significant. The measurement scenario is uniform circular sampling and the frequency of both the transmitted and received signals are assumed to be linear. However, there exists nonlinear phase term in both parts [4]. Estimation and removal of the phase nonlinearity requires priori knowledge of the phase information from both in-phase and quadrature channel. In this project, further efforts need to be made to correct the phase nonlinearity when there is only one channel available.

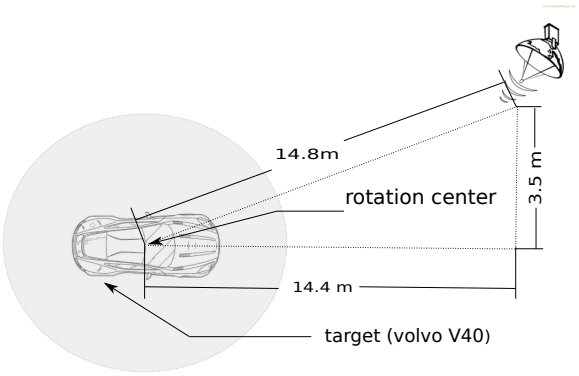

Figure 3.7: Measurement scenario

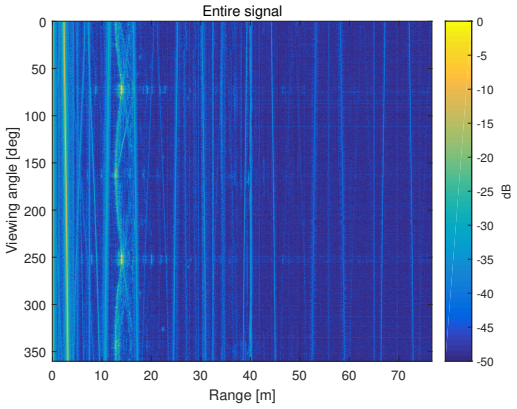

Figure 3.8: Sinogram

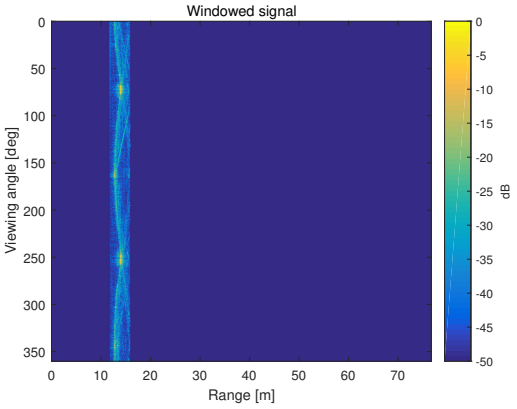

Figure 3.9: Filtered sinogram

3.2 Unequally Spaced FFT (USFFT)

Unequally spaced Fourier transform(USFFT) has become a powerful tool for image reconstruction. Technically speaking, USFFT and GM share the same principle. Both start from interpolating the collected signals, and end with removal of weight function. Unlike Gridding Method, however, USFFT has an advantage in computation speed and the reliability in many different sampling geometries.

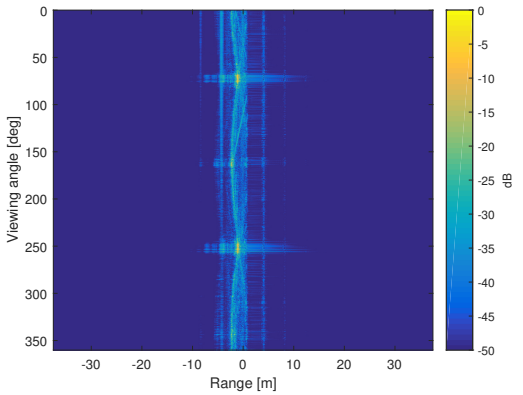

Figure 3.10: Correction of rotation center

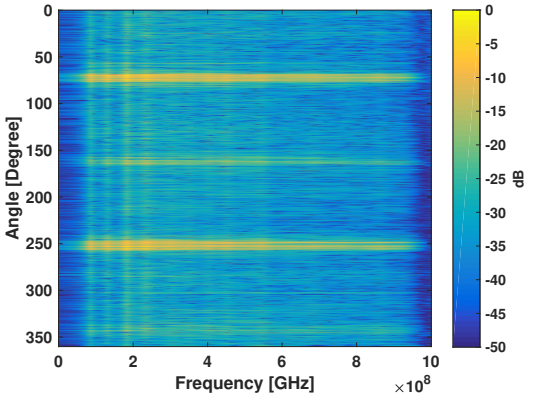

Figure 3.11: Modified measurement in frequency-angle domain

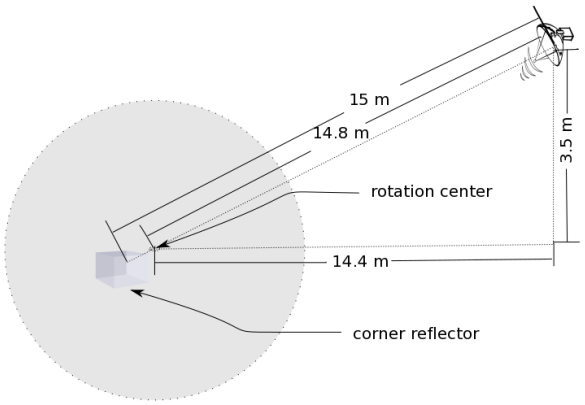

Figure 3.12: Calibration

In previous parts, the sampling geometry is assumed to be circular sampling given in (2.31). USFFT can work under arbitrary sampling so that the support of measurement E^{s} could be arbitrary. In this case, the sampling will always be uniform circular sampling.

The procedure of USFFT is similar to GM. First, a weight function is applied to interpolate the unequally spaced data to uniform Cartesian grid. Then the standard inverse FFT is utilized. Finally, the effect of the weight function is removed by

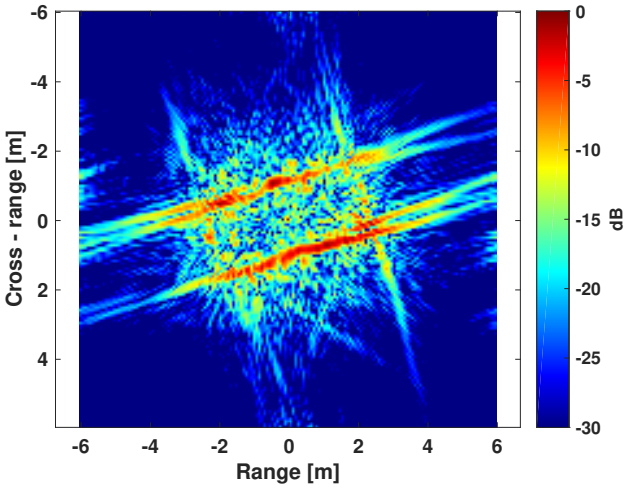

Figure 3.13: Radar signature of Volvo V40

dividing the weight function in spatial domain.

The inverse Fourier transform of the backscattered data is given by:

$$f(\mathbf{x_m}) = \frac{1}{4\pi^2} \sum_{i,l} \mathrm{E}^s(\xi_{i,l}) e^{j\xi_{i,l}\mathbf{x_m}}, \tag{3.9}$$

where $\mathbf{x_m}$ is the Cartesian grid points. Similar to the previous section, the weight function is applied:

$$z(\mathbf{x_m}) = f(\mathbf{x_m})W(\mathbf{x_m}) = \frac{1}{4\pi^2} \int \sum_{i,l} \mathrm{E}^s(\xi_{i,l}) \tilde{W}(\xi - \xi_{i,l}) e^{j\xi\mathbf{x_m}} d\xi. \tag{3.10}$$

The weight function here is still Kaiser-Bessel window. The above integral can be approximated as:

$$z(\mathbf{x_m}) = \sum_n \frac{\Delta\xi_1 \Delta\xi_2}{4\pi^2\eta^2} \sum_{i,l} \mathrm{E}^s(\xi_{i,l}) \tilde{W}(\xi_n - \xi_{i,l}) e^{j\xi_n\mathbf{x_m}}. \tag{3.11}$$

And the uniform Fourier transform is applied. After the interpolation, the effect of weight function will be removed:

$$f(\mathbf{x_m}) = \frac{z(\mathbf{x_m})}{W(\mathbf{x_m})}. \tag{3.12}$$

3.2.1 Simulation

The simulation scenario is exactly the same as the one in GM. Fig.3.14 shows the result of interpolation using USFFT, and fig.3.15 gives the radar signature. Comparing the results by using USFFT to GM, the difference cannot be explained merely by observing the results. However, USFFT takes the advantage over GM in computation speed. We note that the most time consuming part is the interpolation. As C programming could be more efficient, the interpolation part is performed in C using MATLAB Coder toolbox.

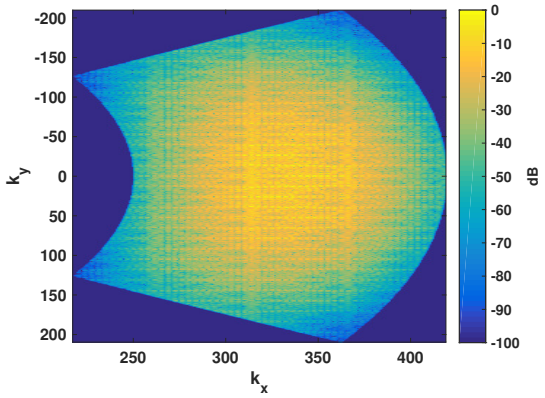

Figure 3.14: The result of interpolation

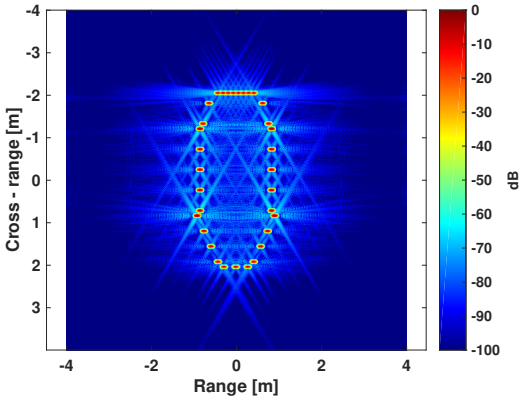

Figure 3.15: Target signature

Table 3.2 shows the comparison of time demanded to generate above target signatures by these two methods. The running time mostly depends on real implementation. In this project, only the interpolation part is developed in C code, and other blocks of the simulation such as the generation of measurement data also take time to wait. Further optimization could be taken to speed up the algorithm.

Table 3.2: Time consumed by two methods

USFFT	38.3696s
GM	47.5422s

3.2.2 Measurement

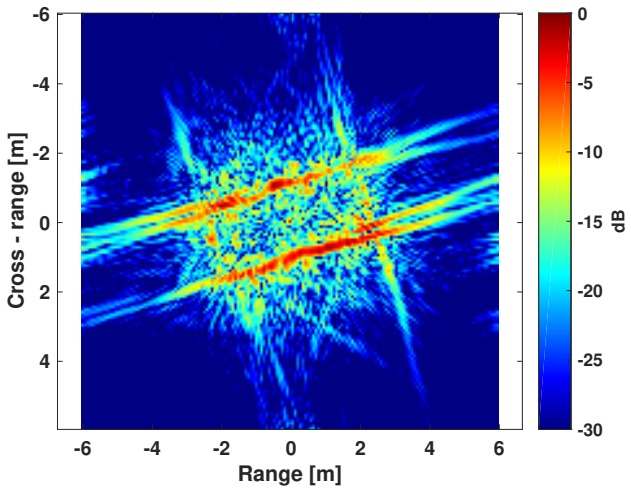

Figure 3.16: Radar signature of Volvo V40

Fig.3.16 shows the radar signature of Volvo V40 by using USFFT. Again, no significant difference can be observed from the measurement results neither. The

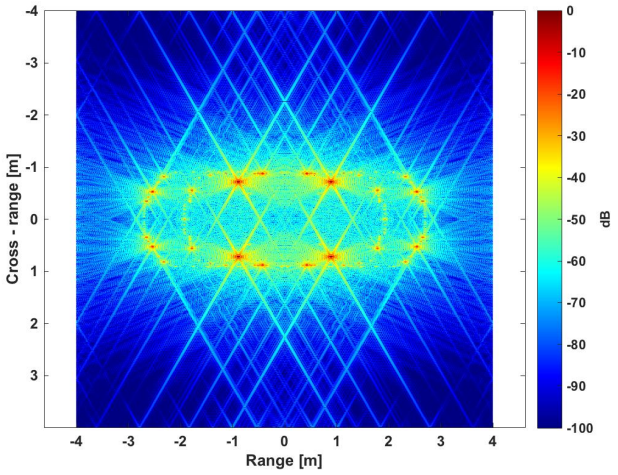

Figure 3.17: Target signature of artificial data

explanation exists in that besides the similarity of interpolation in both methods, the post-processing of the measurement data remains same.

The target signature of Volvo V40 is generated from massive backscattered data and the calculation in this step has already taken up most of the computer memory. It is impossible to do any further process using measurement data with available equipment. Thus, we turn to artificial data generated by electro-magnetic simulation tool and evaluate the target signature. Fig.3.17 shows it. In further process, the l_1 minimization is performed based on artificial data instead.

3.3 l_1-norm Minimization

Linear inverse problem where the solution is assumed to have a sparse representation on some pre-assigned orthonormal basis. In [17], it is proven that replacing the usual quadratic regularizing by weighted penalities on some of the expansions can still compute the regularized solution. They proposed an iterative algorithm with thresholding applied at each iteration step. [1] fulfilled l_1-norm minimization by implement this soft iterative thresholding algorithm.

Consider the optimization problem (2.35)

$$\min_f \|Af - \hat{g}\|_2^2 + \mu \|f\|_1 , \tag{3.13}$$

where f represents the samples $f(x_m)$ on the Cartesian grid x_m in (3.13), and matrix $A = A(m, s) = \mathrm{e}^{-\mathrm{j}x_m \cdot \xi_s}$. Moreover, ξ_s is the uniform polar grid shown in (2.31), and $\hat{g}$ is the vector of all frequency samples, and μ is the threshold to keep the tradeoff between the first term and the second term in (3.13). The above optimization problem aims to minimize the reconstruction error (first term) and keeping the sparse representation signal as much as possible (second term).

In [1] it is shown that the solution to (3.13), the iterative scheme is

$$f^{n+1} = S_\mu((I - T)f^n + f_V), \tag{3.14}$$

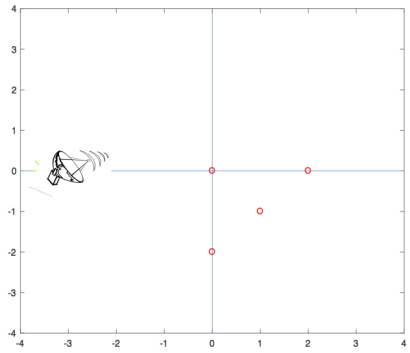

Figure 3.18: Simulation scenario

with I being the identity operator, and S_μ being the soft thresholding operator defined as

$$S_\mu(f)(m) = \max(|f(m)| - \frac{\mu}{2}, 0)\frac{f(m)}{|f(m)|}. \tag{3.15}$$

In (3.14) matrix $T = A^*DA$, and the diagonal matrix $D = q_s\hat{V}(\xi_s)$. Moreover, q_s is the quadrature weight and $\hat{V}(\xi_s)$ is the sampled apodizing window, also the vector $f_V = A^*D\hat{g} = Tf$ is the vector of apodized reconstruction values.

3.3.1 Simulation

This iterative soft thresholding method has an extremely high demand on the memory of the computer, since matrix A is a relatively large matrix being the product of all the frequency samples and angle samples. Therefore, we process some scattering points from the vehicle instead of the whole scattering centers.

Fig.3.18 shows the simulation scenario. There are four scattering points located at specific places in a 2D plane and the radar is lied along the x-axis on the left side. Fig.3.19 is the original ISAR image after implementing USFFT. We have significant side-lobes caused by the limitation of finite bandwidth of radar, as we mentioned before.

For self-driving or other advanced driving techniques, saving time is very important , because the immediate response is needed. Therefore the redundant or useless information such as side-lobes should be decreased or removed. The reason why we implement l_1-norm minimization after radar imaging is because we want to remove the side-lobes caused by limited bandwidth and decrease the redundant information. After running this iterative soft thresholding algorithm for 30 times, side-lobes have been removed, as shown in Fig.3.20. Then after 100 and 160 times iteration, we are also able to remove the part which has less intensity compared to the other part, as shown in Fig.3.21 and Fig.3.22.

As we mentioned in the theory previously, in theory we assume transmitted radar signal has infinite bandwidth leading to the fact that the received radar signal will be a δ function. But in practice, the received radar signal is a sinc function instead of a δ function, because of the limited bandwidth. This is shown in Fig.3.19, the received signal is a circle (sinc function) instead of a dot (δ function). The functionality of l_1-norm minimization is de-convolve the effect caused by radar signature itself.

Certainly we can run more iterations,reducing the diameter of the red circles, but we may lose some useful information. On the other hand, we can also increase the threshold μ, get sparser signal, then we undertake the risk of no useful information left. In this simulation, we choose the threshold $\mu = 0.001 \cdot \max(f_V)$, and stop the iterations at 160 times. These parameters are chosen after several trails which we found out they may give us a good performance.

3.3.2 Measurement

The simulations verifie that the iterative soft thresholding algorithm can remove the redundant information and increase the computational efficiency for further process. However, in our thesis work, the target we focus on mostly is vehicle, so in this part we will show how this algorithm works when the target is the whole vehicle.

One point which cannot be neglected is that processing the whole vehicles will require a great portion of the memory of the computer. As a trade-off, we decrease the image resolution and re-scale the car size by multiplying by 0.1, as shown in Fig.3.23 to Fig.3.24. In Fig.3.23, we set the range extend and cross-range extend as 4 meters and frequency sampling numbers as 1024 and angle sampling numbers as 1404. However, in Fig.3.24, we set the range, and cross-range extend as $0.1 \cdot 4$ meters, and decrease the frequency samplings from 1024 to 100, and at the same time decrease angle samplings from 1404 to 100.

As expected, compared to Fig.3.23, the resolution in Fig.3.24 has been lowered. Nonetheless we can still see the clear sketch of the vehicle. From here on we choose to implement the iterative soft threshold algorithm on Fig.3.24 instead of Fig.3.23.

Similar to previous simulations, in the beginning, the number of iterations is 100. It is obvious that the side-lobes and small intensity points have been removed, as seen in Fig.3.25. Similarly, after 160, 200 and 250 iterations, the results are shown in Fig.3.26,3.27 and 3.28.

Here we still choose the threshold $\mu = 0.001 \cdot \max(f_V)$. The value of threshold μ and the iteration times, mostly depend on the requirement in practice. For example,

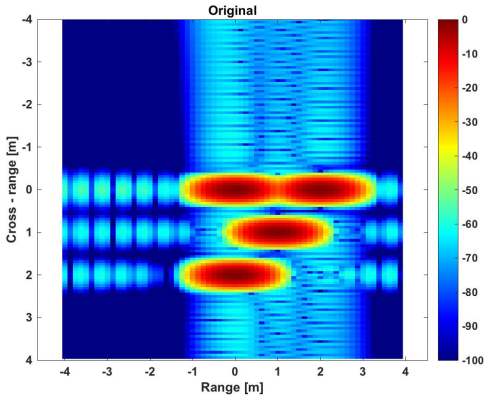

Figure 3.19: Origianl scattering points after reconstruction

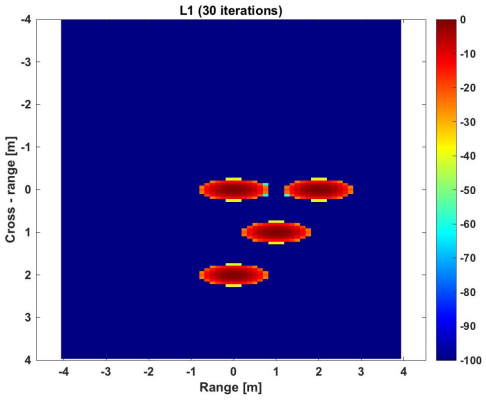

Figure 3.20: Scattering points after 30 times iteration

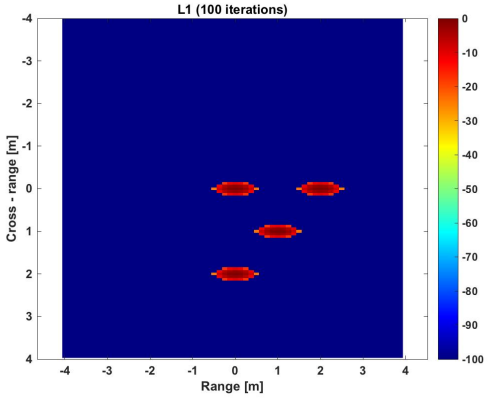

Figure 3.21: Scattering points after 100 times iteration

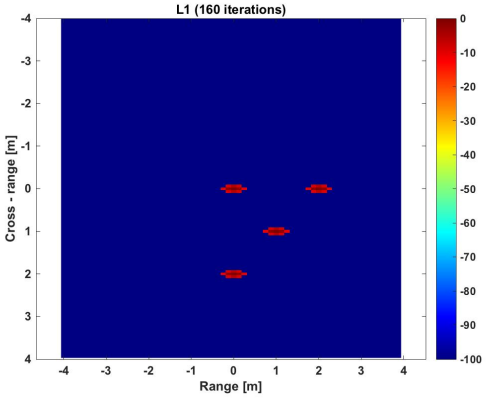

Figure 3.22: Scattering points after 160 times iteration

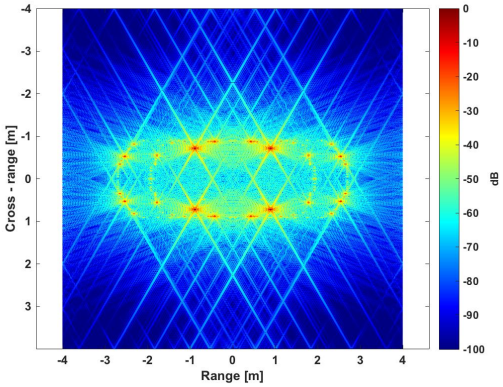

Figure 3.23: Reconstruction image with higher resolution

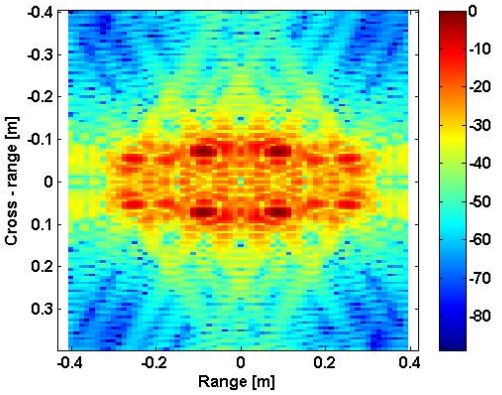

Figure 3.24: Reconstruction image after lowering the resolution

if we want a sparser signal eventually, then both increasing the threshold and iteration times work. On the other hand, if we still want to keep a complete or relative clear sketch of the car, then we should do the opposite way.

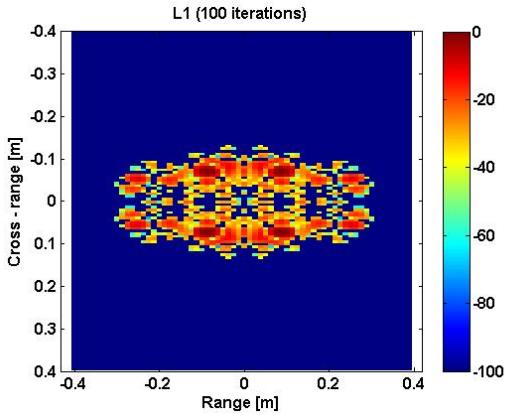

Figure 3.25: Scattering points after 100 times iteration

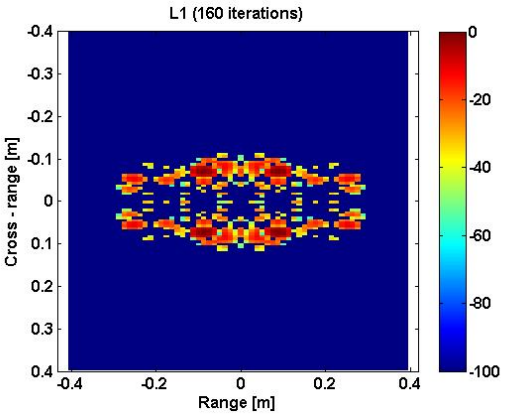

Figure 3.26: Scattering points after 160 times iteration

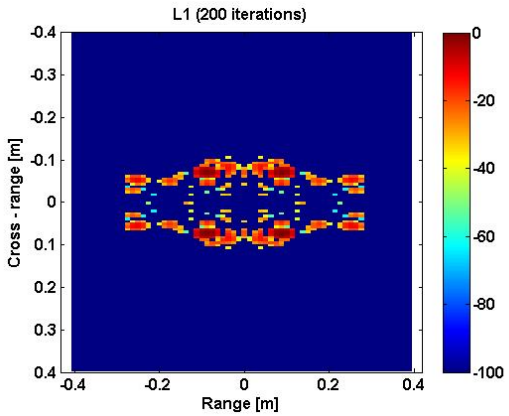

Figure 3.27: Scattering points after 200 times iteration

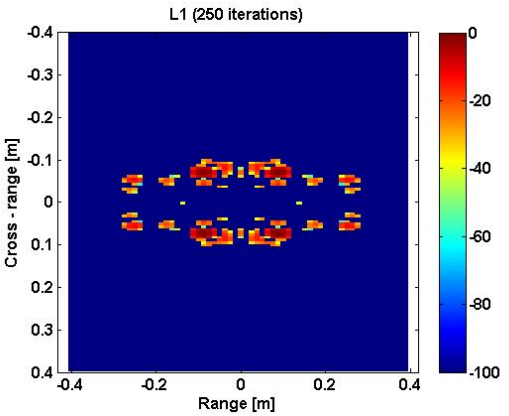

Figure 3.28: Scattering points after 250 times iteration

4
Conclusion

To model the traffic objects, analysis of scattering points is an efficient and powerful approach which can be done by by means of synthetic aperture radar(SAR) imaging and sparse representation. With the help of Fourier reconstruction methods, it is possible to visualize the target signature in an accurate and fast way. The Sparse representation is capable of considerably simplifying the target signature. We can draw the following conclusions:

- Due to the proper interpolation, the backscattered data collected by SAR is re-arranged to uniform Cartesian grid. Thus, the FFT can be applied. These two steps contribute to the success of Gridding Method, and USFFT while directly apply uniform FFT to the backscattered data would be rather time-consuming.
- Scattering centers modeling is capable of describing the target. In this case, the performance of reflectivity depending on the different parts of the vehicle varies with material and the structure. Scattering center modeling may not be helpful in others cases where such condition cannot be satisfied.
- l_1 minimization can significantly reduce the redundancy of the target signature while keep the core information in the model with a user-select parameter. The redundancy here refers to the useless information such as interference and side-lobes. It could bring more convenience for further process.
- The target, Volvo V40, has strong reflectivity on flanks while relatively weaker on head and tail. For further process, it has to be take into consideration when designing vehicular radar system and implementing relevant algorithms to detect objects.

Even though the initial goal of this the work is achieved, there are some limitations unsolved so far due to limited time. It can be believed the solution of these imperfection could boost the overall performance of the model.

- The radar used in this project can only function with one channel, which brings difficulties in nonlinearity correction. Also, there are some significant interference in the measurement. From the near-field reflection shown in the range profile, there are some objects with strong reflectivity closing to radar. Also, some strange curves exist in the sinogram.
- The radar signal used to measure the target has only 1 GHz bandwidth. This leads to significant side-lobes if Fourier reconstruction is applied. Other algorithms could be used if bandwidth condition is not as desired.
- The code generated in this project is mostly developed in MATLAB. Although the most time-consuming part, interpolation, is written in C, which enhances the performance considerably, it is more efficient to rewrite all the code in C.

- Two key parameters in l_1, the iteration index and threshold, are set manually. Finding a smarter way to set these values can also be done in future works.

Bibliography

[1] Andersson, F., Moses, R., and Natterer, F. (2012). Fast Fourier methods for synthetic aperture radar imaging. IEEE Transactions on Aerospace and Electronic Systems, 48(1), 215-229.

[2] Ozdemir, C. (2012). Inverse synthetic aperture radar imaging with MATLAB algorithms (Vol. 210). John Wiley & Sons.

[3] Wang, R., Loffeld, O., Nies, H., Knedlik, S., Hagelen, M., and Essen, H. (2010). Focus FMCW SAR data using the wavenumber domain algorithm. IEEE Transactions on Geoscience and Remote Sensing, 48(4), 2109-2118.

[4] Meta, A., Hoogeboom, P., and Ligthart, L. P. (2007). Signal processing for FMCW SAR. IEEE Transactions on Geoscience and Remote Sensing, 45(11), 3519-3532.

[5] Romberg, J. (2008). Imaging via compressive sampling. IEEE Signal Processing Magazine, 25(2), 14-20.

[6] Dutt, A., and Rokhlin, V. (1993). Fast Fourier transforms for nonequispaced data. SIAM Journal on Scientific computing, 14(6), 1368-1393.

[7] Fourmont, K. (2003). Non-equispaced fast Fourier transforms with applications to tomography. Journal of Fourier Analysis and Applications, 9(5), 431-450.

[8] Fessler, J. A., and Sutton, B. P. (2003). Nonuniform fast Fourier transforms using min-max interpolation. IEEE Transactions on Signal Processing, 51(2), 560-574.

[9] Andersson, F., and Beylkin, G. (2005). The fast Gauss transform with complex parameters. Journal of Computational Physics, 203(1), 274-286.

[10] Schomberg, H., and Timmer, J. (1995). The gridding method for image reconstruction by Fourier transformation. IEEE transactions on medical imaging, 14(3), 596-607.

[11] Gao, L. (2010). Dictionary for Sparse Representation of Chirp Echo in Broadband Radar. arXiv preprint arXiv:1008.0178.

[12] Zhang, L., Xing, M., Qiu, C. W., Li, J., and Bao, Z. (2009). Achieving higher resolution ISAR imaging with limited pulses via compressed sampling. IEEE Geoscience and Remote Sensing Letters, 6(3), 567-571.

[13] Baraniuk, R., and Steeghs, P. (2007, April). Compressive radar imaging. In Radar Conference, 2007 IEEE (pp. 128-133). IEEE.

[14] Andersson, F., Carlsson, M., Tourneret, J. Y., and Wendt, H. (2014). A new frequency estimation method for equally and unequally spaced data. IEEE Transactions on Signal Processing, 62(21), 5761-5774.

[15] Demanet, L., Ferrara, M., Maxwell, N., Poulson, J., and Ying, L. (2012). A butterfly algorithm for synthetic aperture radar imaging. SIAM Journal on Imaging Sciences, 5(1), 203-243.
[16] Huang, K., Aviyente, S. (2007). Sparse representation for signal classification. In Advances in neural information processing systems (pp. 609-616).
[17] Daubechies, I., Defrise, M., and De Mol, C. (2004). An iterative thresholding algorithm for linear inverse problems with a sparsity constraint. Communications on pure and applied mathematics, 57(11), 1413-1457.
[18] Beck, A., and Teboulle, M. (2009). A fast iterative shrinkage-thresholding algorithm for linear inverse problems. SIAM journal on imaging sciences, 2(1), 183-202.
[19] Suksmono, Andriyan Bayu, and Achmad Munir. "Signal processing of range detection for SFCW radars using Matlab and GNU radio." Computer, Control, Informatics and Its Applications (IC3INA), 2014 International Conference on. IEEE, 2014.
[20] Colton, D., and Kress, R. (2012). Inverse acoustic and electromagnetic scattering theory (Vol. 93). Springer Science and Business Media.
[21] D.J.Daniels.Surface-penetrating radar. IEE Press, London,1996.
[22] H.Ling, R.Chou, and S.W.Lee.Shooting and bouncing rays: Calculation the RCS of an arbitrary shaped cavity. IEEE Transactions on Antennas and Propagation 37 (1989) 194-205.
[23] Chen, V. C., Li, F., Ho, S. S., and Wechsler, H. (2006). Micro-Doppler effect in radar: phenomenon, model, and simulation study. IEEE Transactions on Aerospace and electronic systems, 42(1), 2-21.
[24] Boyd, S., and Vandenberghe, L. (2004). Convex optimization. Cambridge university press.